frontiers | Frontiers in Chemical Engineering

TYPE Original Research
PUBLISHED 06 February 2024
DOI 10.3389/fceng.2024.1272152

OPEN ACCESS

EDITED BY
Parasuraman Selvam,
Indian Institute of Technology Madras, India

REVIEWED BY
Xiayi Hu,
Xiangtan University, China
Luis Miguel Madeira,
University of Porto, Portugal

*CORRESPONDENCE
Martin van Sint Annaland,
m.v.sintannaland@tue.nl

RECEIVED 03 August 2023
ACCEPTED 24 January 2024
PUBLISHED 06 February 2024

CITATION
Xin K, Boon J, van Dijk HAJ and van Sint Annaland M (2024), Stability of potassium-promoted hydrotalcites for CO_2 capture over numerous repetitive adsorption and desorption cycles.
Front. Chem. Eng. 6:1272152.
doi: 10.3389/fceng.2024.1272152

Stability of potassium-promoted hydrotalcites for CO_2 capture over numerous repetitive adsorption and desorption cycles

Kun Xin[1], Jurriaan Boon[2], H. A. J. van Dijk[2] and Martin van Sint Annaland[1]*

[1]Chemical Process Intensification, Department of Chemical Engineering and Chemistry, Eindhoven University of Technology, Eindhoven, Netherlands, [2]TNO, Sustainable Technologies for Industrial Processes, Petten, Netherlands

Hydrotalcite-based adsorbents have demonstrated their potential for CO_2 capture, particularly in the sorption-enhanced water-gas shift (SEWGS) process. This study aims to investigate the long-term stability of a potassium-promoted hydrotalcite-based adsorbent (KMG30) over many repetitive cycles under various operating conditions. The stability of the adsorbent, both in terms of its structure and sorption capacity, is examined through multiple consecutive adsorption and desorption cycles. However, it is observed that the capacity for CO_2 adsorption decreases when subjected to many repeated cycles of CO_2 adsorption followed by N_2 flushing, or to many repeated cycles of H_2O adsorption followed by N_2 flushing. In-depth investigations employing various techniques such as thermogravimetric experiments, XRD, BET, and SEM-EDX analyses were conducted to elucidate the underlying phenomena that can explain this observed behavior. The former can be attributed to aggregation of K_2CO_3 from the sorbent during the CO_2 adsorption and N_2 flushing cycles (which can be reversed by re-dispersing the K_2CO_3 either by exposure to air or by processing the sorbent with cycles of CO_2/H_2O adsorption followed by N_2 flushing), whereas the latter is ascribed to the only partial regeneration of the reactive site (referred to site C in earlier work), most likely associated with K_2CO_3 modification on MG30. In this case, morphological changes were found to be insignificant. Remarkable stability of KMG30, as known from SEWGS process studies, was confirmed during cycles of CO_2 adsorption/steam purge. These findings significantly enhance our understanding of the stability of potassium-promoted hydrotalcite-based adsorbents and provide valuable insights for the design of diverse sorption processes.

KEYWORDS

hydrotalcite, potassium carbonate, CO_2 adsorption, stability, TGA, XRD

1 Introduction

Hydrogen possesses significant potential for replacing fossil fuels, and its global demand is projected to increase by an order of magnitude until 2050 (Nuttall and Bakenne, 2020). Currently, the most widely used technology for hydrogen production is conventional steam methane reforming (SMR) (Song et al., 2022), which accounts for nearly half of the global hydrogen demand. The SMR reaction is reversible and highly endothermic, typically

performed at high temperatures ranging from 700°C to 1,000 °C. The resulting syngas is then converted to CO_2 and H_2 through the water-gas shift (WGS) reaction. To achieve high CO conversion, two consecutive reactors with intercooling are commonly employed. Purification of H_2 and CO_2 capture can be accomplished through technologies like pressure swing adsorption (PSA) and absorption with Selexol (Hufton et al., 1999), albeit at the expense of reduced process efficiency (Boon et al., 2016).

The sorption-enhanced water-gas shift (SEWGS) process offers a promising approach for hydrogen production with simultaneous CO_2 removal (van Selow et al., 2009b). It combines the functions of the second WGS reactor and the PSA gas adsorber into a single unit operation. During the WGS reaction, CO_2 is adsorbed on solid materials at temperatures ranging from 350 °C to 550 °C. This *in-situ* CO_2 capture reduces the CO_2 partial pressure in the WGS reactor, promoting a higher conversion of syngas to H_2. Studies have shown that the cost of CO_2 avoidance through SEWGS (Manzolini et al., 2013) can be 35% lower than that achieved by the Selexol process in an integrated gasification combined cycle (IGCC) power plant.

Various materials, including layered double hydroxides (LDHs), MgO, CaO, and alkali ceramic-based materials, have been extensively investigated as adsorbents in SEWGS processes (Wang et al., 2014). The adsorption materials of N-functionalized solid adsorbents (Hu et al., 2020a; Hu et al., 2020b) exhibit very high CO_2 adsorption capacities such as 1.65 mmol CO_2/g at 35 °C with the acid-modified sepiolite with 0.8 g-diethylenetriamine loading (Liu et al., 2018). However, these adsorbents are not suitable for high temperature use due to amine degradation. Hydrotalcites have garnered particular attention due to their reported fast adsorption/desorption rates, stable cyclic CO_2 capacity during adsorption-desorption experiments, excellent mechanical strength under high-pressure steam, and lack of interactions with physically mixed WGS catalysts (Walspurger et al., 2008). The addition of alkali metal salts has been found to effectively enhance the CO_2 adsorption capacity (Sun et al., 2020). In the literature, the adsorption process is typically conducted under different CO_2 partial pressures in a nitrogen mixture, and N_2 flushing or vacuum swing is used to regenerate the sorbent (Rossi et al., 2016; Silva et al., 2017; Rocha et al., 2019; Sun et al., 2020). However, some adsorption sites cannot be fully regenerated using these approaches, necessitating steam regeneration to fully exploit the active sites (Coenen et al., 2017). Steam has been reported to increase the CO_2 adsorption capacity of potassium-promoted hydrotalcites (Maroño et al., 2013), and co-adsorption of CO_2 and H_2O aligns with real-world conditions since a considerable amount of steam is present during WGS.

Currently, the CO_2 adsorption capacity of hydrotalcites is primarily determined through sorption isotherms in short-term breakthrough experiments (Maroño et al., 2013; Rocha et al., 2019) or a few sorption/desorption cycles using the gravimetric method (Xiao et al., 2008; Miguel et al., 2014; Coenen et al., 2018). There have been few studies that have examined the stability of potassium-promoted hydrotalcite during numerous repeated cycles of adsorption and desorption. Wu et al. (Wu et al., 2013) reported a decrease of approximately 7% in CO_2 adsorption capacity after ten cycles of CO_2 adsorption followed by humid helium flushing. Martunus et al. observed a significant drop in CO_2 capacity after 39 cycles of CO_2 adsorption/N_2 flushing, and a gradual decrease after 51 cycles of humid CO_2 adsorption followed by steam purge (Martunus et al., 2012), while Selow et al. found stable cyclic capacity for K_2CO_3-promoted hydrotalcite after 250 cycles of humid CO_2/steam rinse (Van Selow et al., 2009a). The stability of potassium-promoted hydrotalcite during multiple repetitive cycles of adsorption and desorption as well as the mechanisms determining the instability remain unclear. Hence, this study aims to investigate the effects of different long-term operating cycles, such as CO_2 adsorption followed by steam flushing, CO_2 and H_2O co-adsorption followed by N_2 flushing, CO_2 and H_2O co-adsorption followed by steam purge, steam adsorption followed by N_2 flushing, and also CO_2 adsorption followed by N_2 flushing, on the CO_2 capacity and possible morphological changes of potassium-promoted hydrotalcite-based sorbents. This investigation employs thermogravimetric analyses and various characterization techniques, including XRD (X-Ray diffraction), SEM-EDX (scanning electron microscopy-energy dispersive X-ray analysis), ICP-MS (inductively coupled plasma-mass spectrometry), and BET (Brunauer-Emmett-Teller) analyses.

2 Materials and methods

2.1 Materials and preparation method

This study utilized three commercially available adsorbents, namely KMG30 and MG30 obtained from SASOL (Germany), and KSORB obtained from BASF (Germany). Table 1 provides a summary of the material names and compositions (Coenen et al., 2017; Maroño et al., 2013). Taking KMG30 as an example, it is a potassium-promoted hydrotalcite with a Mg/Al molar ratio of 0.54 (weight ratio of 30:70 for $MgO:Al_2O_3$) and a potassium carbonate loading of approximately 17 wt%. KMG30 has been extensively investigated in the literature (Cobden et al., 2007; Boon et al., 2015) and shows promise for industrial applications due to its high mechanical stability and decent CO_2 adsorption capacity (Coenen et al., 2016). The adsorbent, a potassium-promoted hydrotalcite-based material characterized by high MgO content, specifically KMG70 (weight ratio of 70:30 for $MgO:Al_2O_3$) from SASOL, was not included in our current study. Compared with KMG30, KMG70 showed a higher cyclic working capacity due to a higher MgO content. However, slow formation of $MgCO_3$ in the bulk phase was observed for KMG70, which leads to poor mechanical stability and increased CO_2 slip during long-term CO_2/H_2O adsorption and desorption cycles (Jansen et al., 2013; Coenen et al., 2018). Except for anhydrous potassium carbonate (K_2CO_3 ≥99%, Sigma Aldrich), all other materials were crushed and sieved to obtain a particle size fraction ranging from 32 to 90 μm. All materials underwent pre-calcination at 523.15 K for 1 h and 723.15 K for 24 h, and were subsequently stored in a glove box under a N_2 atmosphere prior to use or characterization. The pre-calcination procedure was suggested by the manufacturer (Maroño et al., 2014).

The MG30 adsorbent with a K_2CO_3 loading of 20 wt% was prepared in-house and referred to as 20K-MG30. Two methods, namely the solid-solid mixing method and the impregnation-evaporation method, were employed for its preparation and subsequent characterization. In the first method, 0.8 g of pre-

TABLE 1 Different adsorbent materials used in the experiments.

Material	MgO/Al_2O_3 weight ratio	Mg/Al atomic ratio	K_2CO_3 (wt%)
KMG30	30/70	0.54	17
MG30	30/70	0.54	0
KSORB	0/100	0	20
K_2CO_3	—	—	100

TABLE 2 A comprehensive set of experiments designed to investigate the long-term effects of different operating cycles on the CO_2 sorption capacity of KMG30.

The effects of	No. of Exp.	Experimental description for one cycle	No. of steps	No. of cycles
N_2 flushing and heat treatment	1	$[CO_2 \rightarrow N_2]\times10$ ⇨ heat treatment[a] ⇨ $[CO_2 \rightarrow N_2]\times10$ ⇨ heat treatment ⇨ $[CO_2 \rightarrow N_2]\times10$ ⇨ $[CO_2 \rightarrow N_2]\times10$	4	7
$H_2O \rightarrow N_2$ cycles	2	$[CO_2 \rightarrow N_2]\times10$ ⇨ heat treatment ⇨ $[CO_2 \rightarrow N_2]\times10$ ⇨ heat treatment ⇨ $[CO_2 \rightarrow N_2]\times10$ ⇨ $[CO_2 \rightarrow N_2]\times10$ ⇨ $[CO_2 \rightarrow N_2]\times10$ ⇨ $[CO_2 \rightarrow N_2]\times10$	6	2
	3	$[CO_2 \rightarrow N_2]\times10$ ⇨ heat treatment ⇨ $[CO_2 \rightarrow N_2]\times10$ ⇨ heat treatment ⇨ $[H_2O \rightarrow N_2]\times10$ ⇨ $[CO_2 \rightarrow N_2]\times10$ ⇨ $[H_2O \rightarrow N_2]\times10$ ⇨ $[CO_2 \rightarrow N_2]\times10$	6	2
	4	$[H_2O \rightarrow N_2]\times10$ ⇨ $[CO_2 \rightarrow N_2]\times10$	2	9
	5	$[H_2O \rightarrow N_2]\times10$ ⇨ $[H_2O \rightarrow N_2]\times10$ ⇨ $[H_2O \rightarrow N_2]\times10$ ⇨ $[H_2O \rightarrow N_2]\times10$ ⇨ $[CO_2 \rightarrow H_2O]\times20$	5	1
CO_2 and H_2O in the same [adsorption→ desorption]	6	$[CO_2 \rightarrow H_2O]\times10$ ⇨ heat treatment ⇨ $[CO_2 \rightarrow H_2O]\times10$ ⇨ heat treatment ⇨ $[CO_2 \rightarrow H_2O]\times10$ ⇨ $[CO_2 \rightarrow H_2O]\times10$ ⇨ $[CO_2 \rightarrow H_2O]\times10$ ⇨ $[CO_2 \rightarrow H_2O]\times10$ ⇨ $[CO_2 \rightarrow N_2 \rightarrow H_2O \rightarrow N_2]\times6$ ⇨ $[CO_2 \rightarrow N_2]\times10$ ⇨ $[H_2O \rightarrow N_2]\times10$ ⇨ $[CO_2 \rightarrow N_2]\times10$	10	1.5[b]
	7	$[CO_2/H_2O \rightarrow N_2]\times10$	1	6
	8	$[CO_2/H_2O \rightarrow H_2O]\times10$	1	6

[a]Heat treatment is not numbered when counting steps.
[b]Half of the first cycle is repeated.

calcined MG30 and 0.2 g of anhydrous K_2CO_3 were mechanically stirred together. As for the latter method, 0.4 g of pre-calcined MG30, 0.1 g of anhydrous K_2CO_3, and 5.0 g of water were magnetically stirred at 353.15 K until a paste was formed. The solid material prepared using both methods underwent consecutive calcination steps at 363.15 K for 6 h, 473.15 K for 6 h, and 873.15 K for 3 h.

2.2 Thermogravimetric experiments

To investigate the long-term effects of different operating cycles, particularly those involving steam, on K_2CO_3-promoted hydrotalcite, a series of experiments was conducted using a custom-built thermogravimetric analysis (TGA) setup under atmospheric pressure. Approximately 100 mg of solid sample was placed in a porous ceramic basket within a quartz reactor (inner diameter approximately 15 mm). The sample was subjected to different gases with a total flow rate of 500 Nml/min. A thermocouple was positioned near the sample to accurately control the reaction temperature. The weight change of the sample was measured using a microbalance (CI-Precision MK2-5M) with a sensitivity of 0.1 μg. The balance head temperature was kept constant, and it was continuously purged with a constant flow of N_2 to protect the balance and ensure accurate mass readings.

The experimental setup, including the use of a Bronkhorst controlled evaporator mixer (CEM) for generating N_2-containing steam, sample lines wrapped with heat wires and insulation materials to prevent steam condensation, and the absence of mass transfer limitations for CO_2 adsorption by KMG30, has been previously published by our group (Coenen et al., 2016). The experiments for KMG30 are summarized in Table 2. Before each experiment, a pre-calcined sample underwent a pretreatment step with N_2 flushing at 873.15 K for 2 h. Each experiment consisted of multiple steps, indicated by hollow arrows, such as Step 1 ⇨ heat treatment ⇨ Step 2 ⇨ Step 3 ⇨ heat treatment ⇨ Step 4, and so on. A heat treatment process involved N_2 flushing to regenerate the sorbent at 873.15 K for 2 h but was not considered when numbering the steps. The sorbent after the heat treatment process is referred to as the heat-treated sorbent.

A standard adsorption step, such as Step 1/2/3/4, is denoted as [Procedure 1→Procedure 2] × (number of repetitions), where each procedure lasted for 30 min and the procedures in the square brackets were cyclically repeated at 673.15 K. For the procedures in the square brackets, the CO_2 partial pressure in all CO_2-containing gases was fixed at 0.15 bar, while the H_2O partial pressure in all H_2O-containing gases

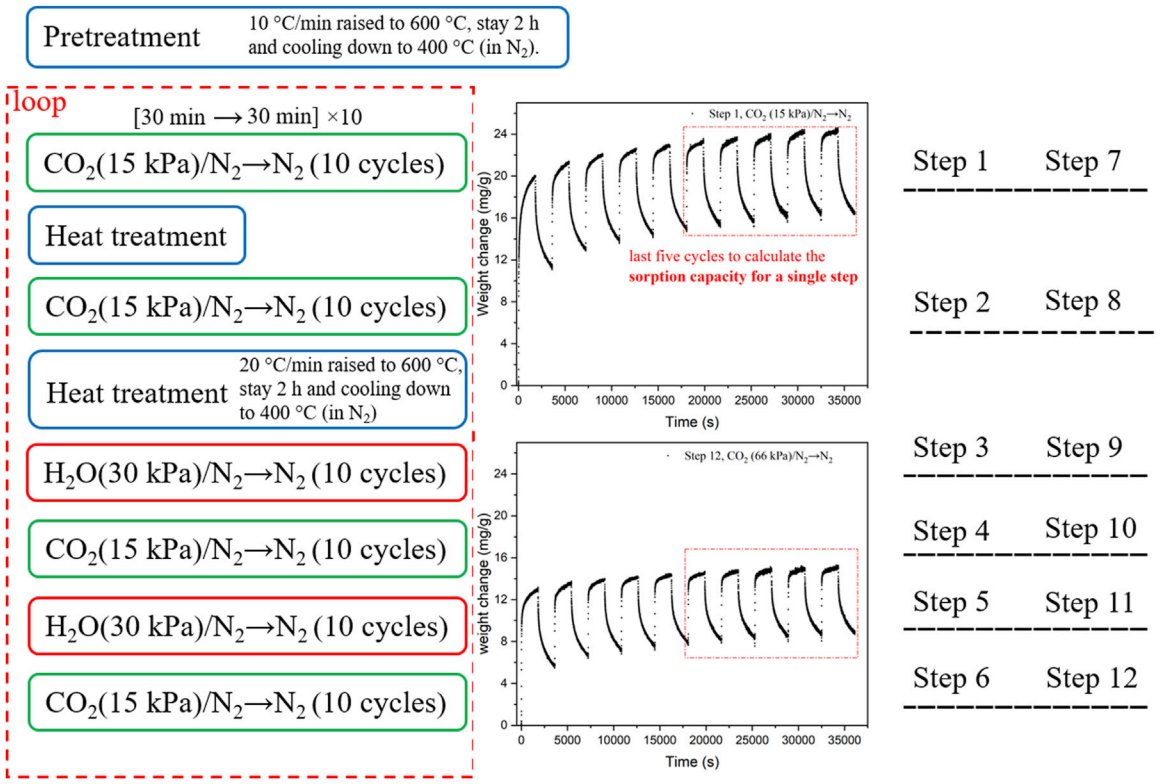

FIGURE 1
Schematic diagram of Exp. 3.

was kept at 0.30 bar. The ratio of steam to CO in a water gas shift reactor is normally between 2:1 and 3:1 (Ebrahimi et al., 2020). The remaining gas consisted of N_2. The adsorption/desorption capacity for a single procedure was defined by Eq. (1), whereas the cyclic working capacity for an adsorption-desorption cycle, such as [CO_2→N_2], was defined by Eq. (2). The average cyclic working capacity of the last 5 measurements ([CO_2→N_2] × 5) for each step was reported as the sorption capacity for that step. The sorbent cyclic capacity was based on the sample mass after the pretreatment step. It is worth noting that in Step 7 of Exp. 6, that consisted of four steps ([CO_2→N_2→H_2O→N_2] × 6), but only the sorption capacity for a single procedure was considered. A schematic diagram of Exp. 3 is shown in Figure 1.

$$q_{CO_2}(half\ cycle) = \frac{\Delta m(half\ cycle)}{M_{CO_2}{}^{*}m_{pretreated\_sample}} \quad (1)$$

$$q_{CO_2}(cyclic) = \frac{\Delta m(ads) + \Delta m(des)}{2^{*}M_{CO_2}{}^{*}m_{pretreated\_sample}} \quad (2)$$

To gain a better understanding of the sorption performance of KMG30, some experiments in Table 2 were conducted for MG30, KSORB, and K_2CO_3. One experiment, denoted as [CO_2→N_2→H_2O→N_2]×6, was carried out to determine the adsorption capacities of CO_2 on different sites. In this experiment, part of the adsorbed CO_2 could be easily removed by reducing the CO_2 partial pressure in the gas phase through N_2 flushing (second step), while the remaining adsorbed CO_2 required reaction with steam (H_2O purge in step 3) for removal. Experiments of [CO_2→H_2O]×40 and [CO_2→N_2]×50 were performed to assess the potential loss in sorption capacity over time. Similar to the experiments conducted with KMG30, the CO_2 partial pressure in all CO_2-containing gases in these experiments was fixed at 0.15 bar, and the H_2O partial pressure in all H_2O-containing gases was fixed at 0.30 bar.

2.3 Sample characterization

The hydrotalcite-based materials were subjected to multiple adsorption/desorption cycles within the TGA setup. After each cycle, the samples were promptly transferred for characterization. The morphological changes of the sorbents were investigated using various techniques. XRD analysis was performed using a Rigaku Miniflex 600 instrument with an air-sensitive sample holder to determine characteristic reflections. BET analysis was conducted using a Thermo Fischer Surfer instrument to determine the BET surface area and BJH (Barrett-Joyner-Halenda) pore size distribution. SEM-EDX analysis was carried out using a Thermo Scientific Phenom ProX instrument, and elemental compositions were determined using an Agilent 4200 MP-AES (microwave plasma atomic emission spectroscopy) instrument. Working cycles of H_2O adsorption→N_2 flushing, CO_2 adsorption→H_2O purge, CO_2/H_2O co-adsorption→N_2 flushing, CO_2/H_2O co-adsorption→H_2O purge and CO_2 adsorption→N_2 flushing were involved for treatments. The preparation procedures for the hydrotalcite-based material (KMG30) and the characterization techniques used are summarized in Supplementary Table S1.

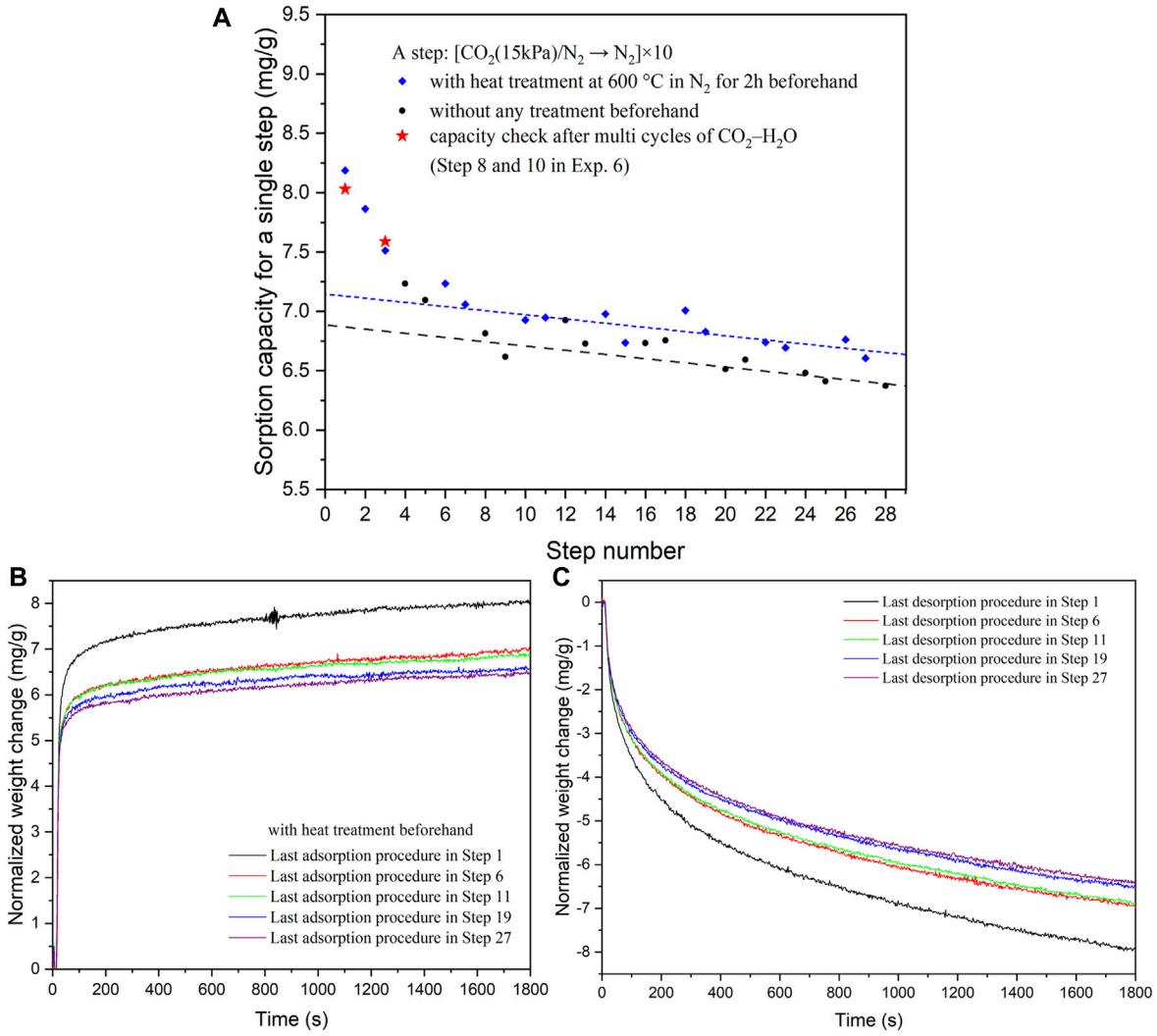

FIGURE 2
(A) Sorption capacities (at 400°C) of CO_2 on KMG30 for different steps in Exp. 1. **(B)** Adsorption kinetics of the last procedures in Steps 1, 6, 11, 19 and 27 in Exp. 1 (steps with heat treatment beforehand). **(C)** Desorption kinetics of the last procedures at 400°C in Steps 1, 6, 11, 19 and 27 in Exp. 1.

3 Thermogravimetric analysis of adsorption/desorption cycles

The impact of different adsorption/desorption cycles on the stability of the adsorption capacities of KMG30 was analyzed and discussed. Section 3.1 focuses on the cycles of dry adsorption/N_2 flushing and heat regeneration procedure. Sections 3.2, 3.3, 3.4, and 3.5 discuss the cycles of H_2O adsorption/N_2 flushing, CO_2 adsorption/steam purge, CO_2 and H_2O co-adsorption/N_2 flushing, and CO_2 and H_2O co-adsorption/steam purge, respectively. Furthermore, in Section 3.6, the performance of MG30 and K_2CO_3 under specific adsorption/desorption cycles is examined.

3.1 Dry adsorption/N_2 flushing and heat treatment

To validate the accuracy of the TGA setup, the cyclic capacity of CO_2 (at 66.6 kPa) was compared with literature values. The reported literature values for KMG30 range between 12 and 13 mg/g (Coenen et al., 2017), whereas our experimental value was found to be 12.2 mg/g (Supplementary Figure S1). In Experiment 1, CO_2 was adsorbed from a CO_2/N_2 mixture at 400°C, followed by N_2 flushing at the same temperature. Thermal regeneration was optionally employed between adjacent steps to further regenerate the sorbent. As depicted in Figure 2, although the sample was regenerated at 600 °C before Steps 2 and 3, the sorption capacity exhibited a relatively rapid drop in the first five steps. Subsequently, it decreased slowly at a rate of approximately 0.018 mg/g per step, as indicated by the dashed lines in the figure. Regarding the two adjacent blue rhombus-shaped markers (indicating steps with prior heat treatment) after Step 5, the first blue rhombus was higher than the preceding black point, while the second rhombus was lower than the first one in most cases. The heat treatment (at 600 °C) only partially restored a sorption capacity of 0.25 mg/g (the distance between the two dashed lines). In the adsorption-desorption process, a continuous loss in sorption capacity was observed when only N_2 flushing and/or thermal swing was employed for sorbent regeneration.

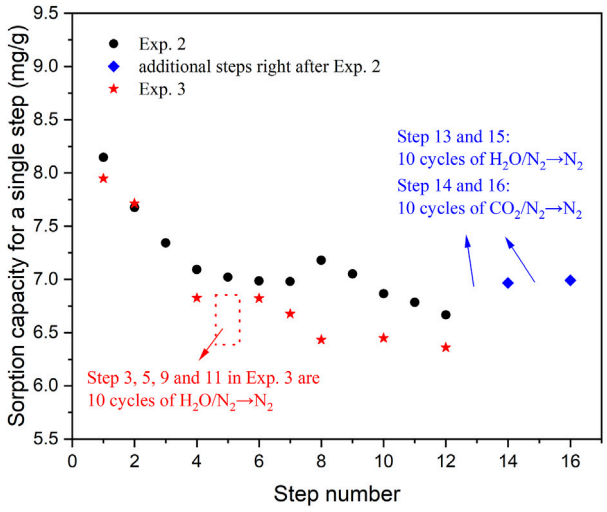

FIGURE 3
The sorption capacity of CO_2 on KMG30 for different steps in Exp. 2 and 3, to investigate the effects of cycles of steam purge/N_2 flushing.

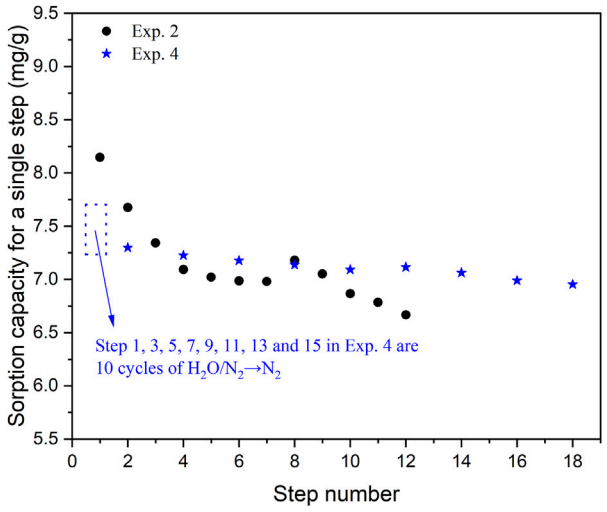

FIGURE 4
The sorption capacity for different steps in Exp. 2 and 4, to investigate the effects of cycles of steam purge/N_2 flushing.

This continuous loss in sorption capacity can be attributed to differences in the kinetics of sorption and desorption. As shown in Figures 2B,C, rapid mass changes occurred at the beginning of the procedures, where approximately 90% and 60% of CO_2 were adsorbed or desorbed within the first 200 s, respectively. Subsequently, CO_2 was only slowly adsorbed by KMG30 (Figure 2B), probably related to the formation of bulk carbonates, while the desorption from the sorbent still occurred at faster rates (Figure 2C). During the last 10 min (1200–1800 s), weight increases of 0.1–0.2 mg/g were observed for the adsorption curves, while weight decreases of 0.4–0.7 mg/g were observed for the desorption curves. Thus, the slow kinetics of the desorption is limiting the cyclic working capacity of KMG30. The reduced half-cycle capacity during the desorption procedures (from Steps 1 to 27 in Figure 2C) accounted for the loss in sorption capacity during multiple cycles of CO_2 adsorption followed by N_2 purge. Similar phenomena were also observed for the steps without heat treatment beforehand (black points in Figure 2). The adsorption and desorption kinetics of these steps are summarized in Supplementary Figure S2.

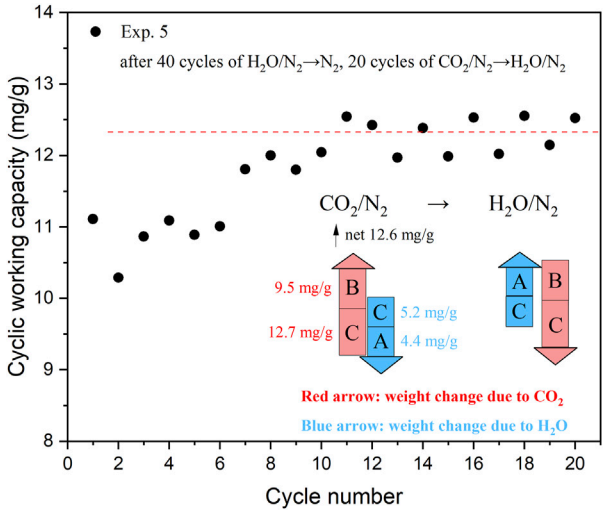

FIGURE 5
The cyclic capacity for different cycles in the last two steps of Exp. 5, to investigate whether the loss of sorption capacity caused by steam purge/N_2 flushing cycles is reversible.

3.2 Effects of H_2O adsorption/N_2 flushing cycles

Exp. 2–5 were conducted to examine the impact of [$H_2O \rightarrow N_2$] cycles. Exp. 2 was similar to Exp. 1, where the CO_2 is adsorbed at 400 °C and desorbed with N_2 flushing at the same temperature. Thermal regeneration was implemented before Steps 1, 2, 3, and 8, 9. Exp. 3 was a modification of Exp. 2, where Steps 3, 5, and 9, 11 consisted of 10 cycles of H_2O adsorption/N_2 flushing. The results for Exp. 2 and 3 are presented in Figure 3. The findings of Exp. 2 were consistent with Exp. 1, with a rapid decrease in sorption capacity during the first 5 steps, and the increased capacity in Step 8 was attributed to the pre-treatment. For Exp. 2 and 3, comparable sorption capacities were observed in Steps 1 and 2. The focus was on the difference between the two experiments. Following 10 cycles of [$H_2O/N_2 \rightarrow N_2$] in Step 3 of Exp. 3, the sorption capacity decreased from 7.7 mg/g in Step 2–6.8 mg/g in Step 4. In Exp. 2, the capacity decreased from 7.7 mg/g in Step 2–7.3 mg/g in Step 3. This finding is intriguing as it is commonly believed that steam can further regenerate the sorbent through reaction with the carbonate (Coenen et al., 2017). This holds true when considering the capacities of Steps 8, 10, and 12 in Exp. 3, where similar values were obtained, indicating that the [$H_2O \rightarrow N_2$]×10 step helped maintaining the sorption capacity. Similar findings were observed in the additional tests following Step 12 in Exp. 2. As shown in

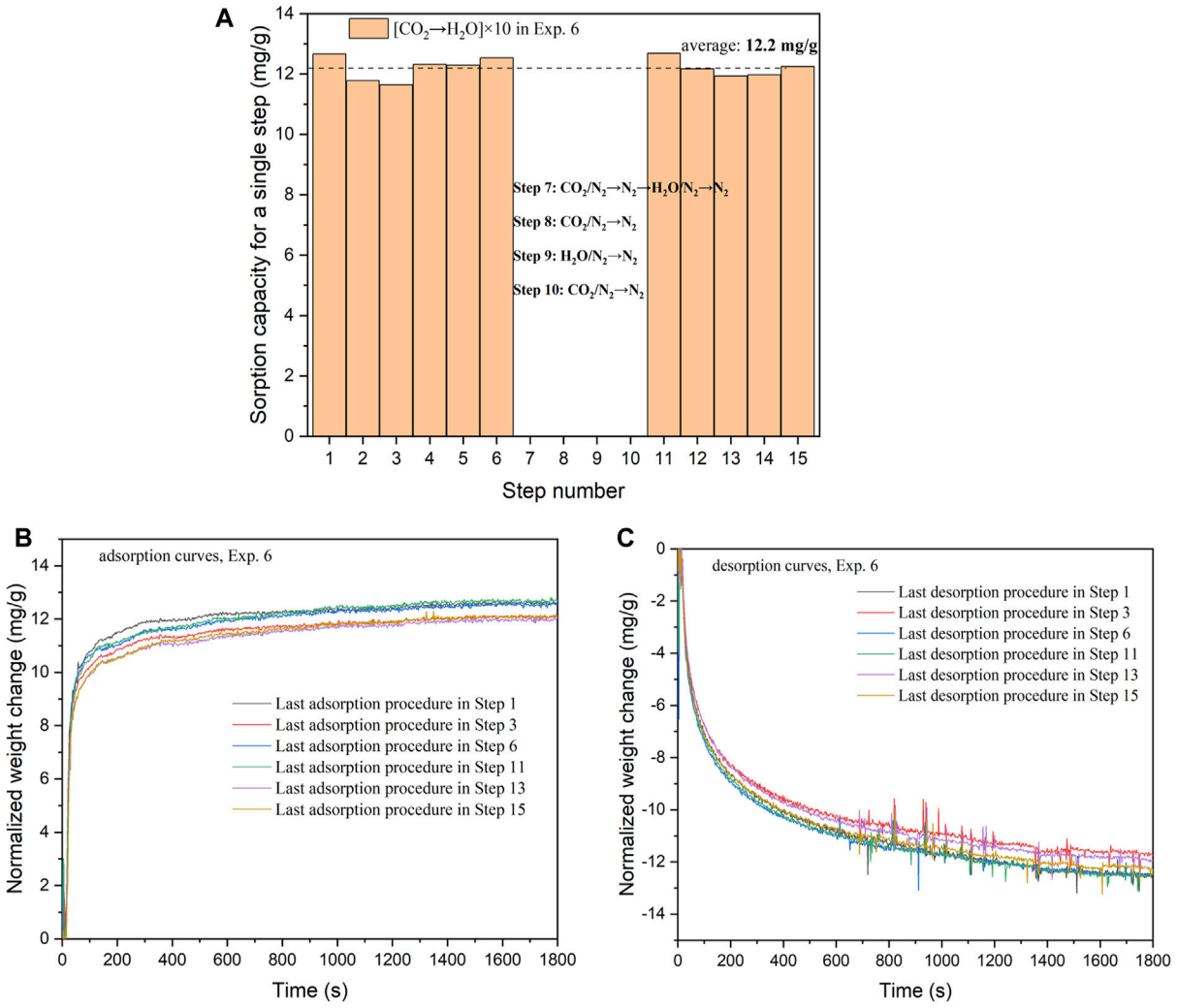

FIGURE 6
(A) The sorption capacities on KMG30 for different steps (one step: [CO_2→H_2O]×10) in Exp. 6. **(B)** Adsorption kinetics of the last procedures at 400 °C in Steps 1, 6, 11, 13 and 15 (Exp. 6). **(C)** Desorption kinetics of the last procedures at 400 °C in Steps 1, 6, 11, 13 and 15 (Exp. 6).

Figure 3, the sorption capacity in Step 14 was higher than that in Step 12, and comparable values were found for Steps 16 and 14. Therefore, early exposure to steam purge/N_2 flushing cycles led to a capacity loss of 0.5 mg/g for KMG30. However, if the sorbent had already undergone 80 cycles of CO_2 adsorption/N_2 flushing, cycles of steam purge/N_2 flushing would help restoring the sorbent capacity.

In Exp. 4, the sorbent was initially subjected to 10 cycles of steam purge/N_2 flushing to validate the findings. As depicted in Figure 4, the sorption capacity in Step 2 of Exp. 4 was 7.3 mg/g, compared to a value of 8.2 mg/g for Step 1 in Exp. 3. This indicates a decrease of 0.9 mg/g in the sorption capacity of CO_2 on KMG30 when cycles of steam purge/N_2 flushing are applied at the beginning. However, a gradual decline in sorption capacities from Step 2 to Step 16 was observed, and it was evident that the blue stars mostly exceeded the black points after Step 3, suggesting that cycles of steam purge/N_2 flushing could restore the capacity subsequently. A comparison diagram illustrating the adsorption kinetics of Step 2 in Exp. 4 with the kinetics of Steps 1 and 2 in Exp. 2 is presented in Supplementary Figure S3A. Apart from the smaller half-cycle capacity for Step 2 in Exp. 4, the shapes of the curves were similar. The same trend was observed for the desorption kinetics (Supplementary Figure S3B). Therefore, after undergoing cycles of steam purge/N_2 flushing, the CO_2 adsorption mechanism remains unchanged while the number of adsorption sites decreases, resulting in a smaller half-cycle capacity for both the adsorption and desorption procedures.

In Exp. 5, the sorbent was subjected to 40 cycles of steam purge/N_2 flushing, followed by 20 cycles of CO_2 adsorption/steam purge. Surprisingly, the cyclic capacity continued to increase throughout the cycles until reaching a constant value of approximately 12.3 mg/g. This trend is in stark contrast to the decreasing trend observed in cycles of CO_2 adsorption/N_2 flushing (Figure 2A). The final stable value is significantly higher than the CO_2 sorption capacity observed in Exp. 4 (around 7.0 mg/g). This indicates the presence of different CO_2 adsorption sites, some of which can only be regenerated using steam (Coenen et al., 2017). The descriptions of the adsorption sites (Sites A and C for H_2O, Sites B and C for CO_2) following the work of

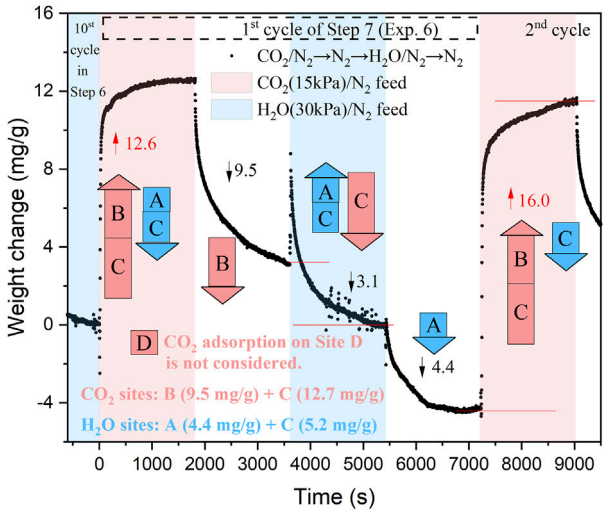

FIGURE 7
Analysis of adsorption capacities of CO_2 and H_2O on different sites of KMG30 (first cycle of Step 7 in Exp. 6).

Coenen et al. are presented in Supplementary Figure S4. The cyclic capacities of last five cycles in Figure 5 are consistent with the sorption capacities for the CO_2 adsorption/steam purge cycles in Section 3.3, showing that the loss of sorption capacity of KMG30 could be restored by subjecting it to cycles of CO_2 adsorption/steam purge. A detailed calculation procedure for the capacities of CO_2 and H_2O on different sites is presented in the next section.

3.3 Dry adsorption/steam purge

In Exp. 6, the sorbent stability under cycles of CO_2 adsorption/steam purge was tested. Cycles of [CO_2→N_2→H_2O→N_2] were employed to determine the adsorption capacities of CO_2 and H_2O in different sites. Following multiple cycles of CO_2 adsorption/steam purge, cycles of [CO_2→N_2] were performed to compare the sorption capacities of CO_2 with those obtained in Exp. 1.

From Figure 6, it can be observed that the sorption capacities of Steps 1–6 and 11–15 exhibit variations around 12.2 mg/g. KMG30 appears to demonstrate remarkable stability during cycles of CO_2 adsorption/steam purge. This stability can be attributed to the rapid kinetics of both the adsorption and desorption processes. Over the last 200 s, the weight increases in the adsorption curves and weight decreases in the desorption curves are approximately 0.04 mg/g and 0.08 mg/g, respectively. These weight changes are insignificant when compared to the overall mass change of approximately 12 mg/g throughout the entire adsorption/desorption period (1800 s). Furthermore, unlike the declining trend in half-cycle capacities observed from Step 1 to Step 27 in Exp. 1 (Figure 2), there is no consistent decreasing or increasing trend in half-cycle capacities from Step 1 to Step 15 in Exp. 6 (Figures 6B,C). For instance, the curves of Step 1 overlap with the curves of Step 11.

Step 7 in Exp. 6 involves six cycles of [CO_2→N_2→H_2O→N_2], which are conducted to measure the adsorption capacities of CO_2 and H_2O on different sites. In this process, the H_2O adsorbed on Site A and CO_2 adsorbed on Site B can be regenerated when the partial pressures of the adsorbed species in the gas phase decrease. On the other hand, H_2O and CO_2 adsorbed in Site C can only be replaced by each other. Specifically, CO_2 will desorb from Site C only if steam is present in the gas phase and the partial pressure of CO_2 decreases. The interchange between CO_2 and H_2O in Site C can be represented by Eqs (3), (4). The final step, Step 6, involves steam purge. The first cycle of Step 7 is depicted in Figure 7. During this cycle with CO_2 feed, H_2O is desorbed from both Sites A and C, while CO_2 is adsorbed on Sites B and C. The specific weight changes observed in Figure 7 are used to determine the sorption capacities of Sites A, B, and C.

During the steam purge, although some H_2O (4.4 mg/g) is adsorbed on Site C, there is a simultaneous exchange (resulting in a net weight loss of (3.1 mg/g)) of CO_2 and H_2O on Site C. The sorption capacities of CO_2 and H_2O on Site C can be determined from this net loss using Eqs (3), (4). The final results are presented in Figure 7, which accurately describe the entire figure. For more detailed information on the adsorption sites of a hydrotalcite-based adsorbent for CO_2 and H_2O adsorption, please refer to the work by Coenen et al. (Coenen et al., 2017).

$$Site\ activation\text{:}\ C[\bullet]O + H_2O \rightarrow C[(OH)_2] \quad (3)$$

$$Site\ exchange\text{:}\ C[(OH)_2] + CO_2 \leftrightarrow C[CO_3] + H_2O \quad (4)$$

The sorption capacities of Steps 8 and 10 in Exp. 7, indicated by red stars in Figure 2A, are consistent with the sorption capacities of Steps 1 and 3 in Exp. 1. Even after multiple cycles of CO_2 adsorption and steam purge, the sorption capacities of CO_2 remain the same as those observed with fresh KMG30. This further demonstrates the exceptional stability of KMG30 under cycles of CO_2 adsorption and steam purge. Furthermore, the sorption capacity of CO_2 in Site B is determined to be 9.5 mg/g according to Figure 7. In contrast, the sorption capacity of Step 1 in Exp. 1 (Figure 2A) is significantly lower, approximately 8.0 mg/g. Upon examining the cyclic capacities of the ten cycles in Step 1 of Exp. 1 (Supplementary Figure S5), the desorption capacities decrease from 9.1 to 8.0 mg/g, all of which are smaller than the determined CO_2 capacity in Site B. One possible reason for this difference is that, apart from Sites B and C, Site D also contributes to CO_2 adsorption (Coenen et al., 2017). CO_2 can be desorbed from Site D under N_2 flushing. Consequently, the method used to determine the capacity of Site B may not be sufficiently accurate. However, since the primary objective of this study is to investigate the long-term stability of KMG30 under various operational cycles, in which it will remain occupied throughout, Site D is not considered further. Another reason for the disparity could be that the sorption capacity on Site B increases during cycles of CO_2 adsorption and steam purge.

3.4 CO_2 and steam co-adsorption/N_2 flushing

In Exp. 7, the sorbent stability under cycles of co-adsorption of CO_2 and H_2O/N_2 flushing was investigated. The results are summarized in Figure 8. The cyclic capacities exhibit a gradual decrease and eventually stabilize at around 15.1 mg/g from Cycles 1 to 60 (Steps 1–6). The stable performance can be attributed to the rapid desorption kinetics, as observed in Figures 8B,C. Over the last 200 s, the weight increases in the

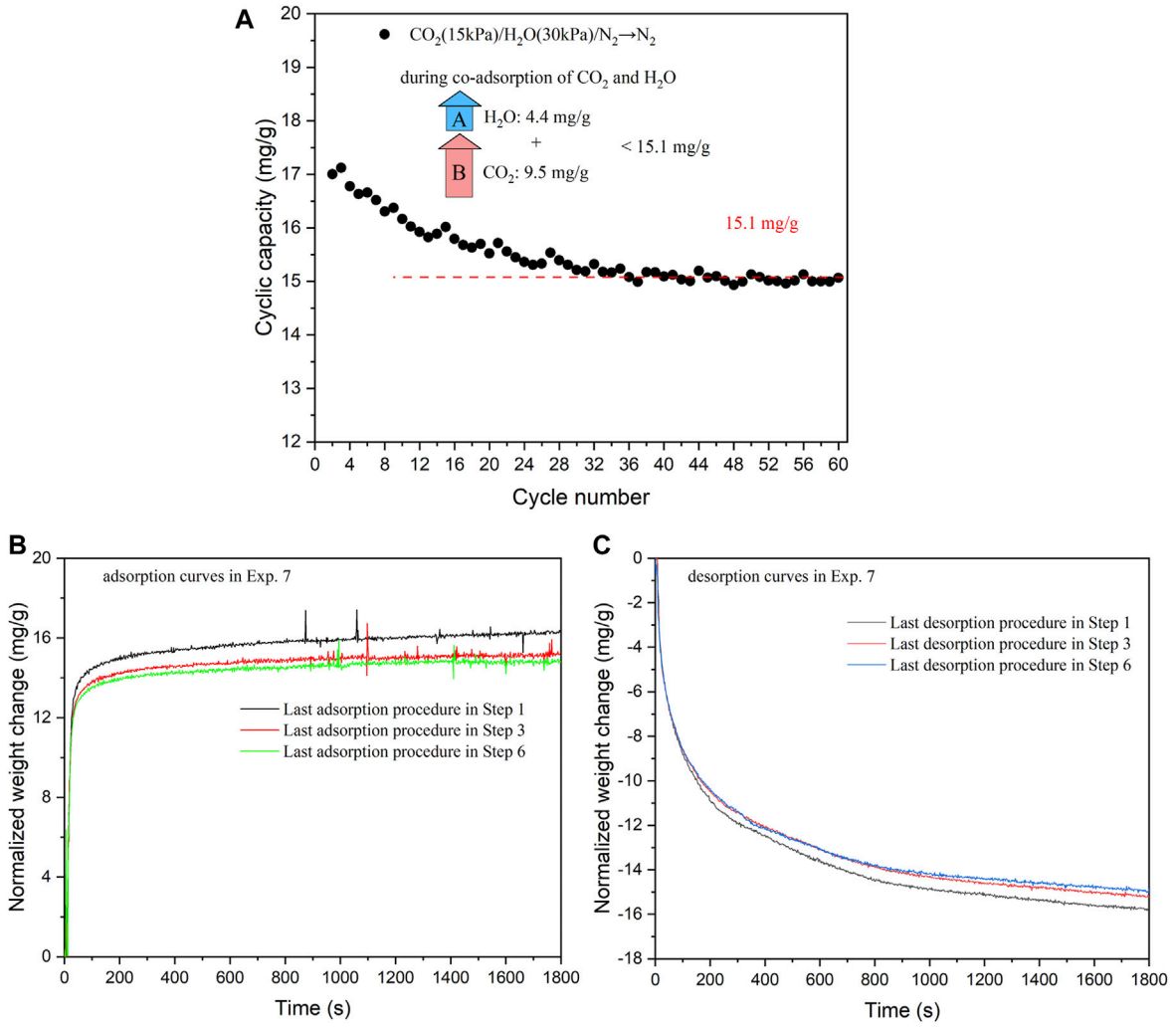

FIGURE 8
(A) Cyclic capacities of all the cycles in Exp. 7 (co-adsorption of CO_2 and H_2O/N_2 flushing on KMG30 at 400 °C). **(B)** Adsorption kinetics of the last procedures in Steps 1, 3 and 6 (Exp. 7). **(C)** Desorption kinetics of the last procedures in Steps 1, 3 and 6 (Exp. 7).

adsorption curves and weight decreases in the desorption curves are approximately 0.10 and 0.15 mg/g, respectively. These weight changes, which are of comparable magnitudes, are insignificant when compared to the overall mass change of around 15 mg/g during the entire adsorption/desorption period (1800 s). The gradual decrease in sorption capacities observed during the initial 30 cycles may be associated with the slightly slower desorption kinetics compared to the adsorption kinetics, as well as some small morphological changes of KMG30.

3.5 CO_2 and steam co-adsorption/steam purge

In Exp. 8, the sorbent stability was tested under cycles of co-adsorption of CO_2 and H_2O/steam purge. The results are summarized in Figure 9, where the cyclic capacities gradually decrease and stabilize around 14.6 mg/g from Cycles 1 to 60 (Steps 1–6). The stable performance is also attributed to the fast desorption/adsorption kinetics exhibited under the working conditions. Figures 9B,C illustrate the adsorption and desorption kinetics, respectively. During the last 200 s of the process, the weight increases in the adsorption curves and weight decreases in the desorption curves are approximately 0.10 and 0.25 mg/g, respectively. Once again, these weight changes, which are of similar magnitudes, are insignificant when compared to the overall mass change of around 15 mg/g during the entire adsorption/desorption period (1800 s).

KMG30 demonstrates stability under cycles of CO_2 adsorption/steam purge, cycles of CO_2 and H_2O co-adsorption/N_2 flushing, and cycles of CO_2 and H_2O co-adsorption/steam purge. However, a noticeable decrease in sorption capacities is observed during cycles of CO_2 adsorption/N_2 flushing, which can be attributed to the difference in desorption kinetics. The summary of sorption capacities for different adsorption/desorption cycles was presented in Supplementary Table S2. From a microscopic perspective, Site C appears to play a crucial role in maintaining stable sorption capacities for CO_2. To ensure stable performance, it is necessary to remove CO_2 from Site C. In the cycles of CO_2 adsorption/N_2 flushing, only Site B of KMG30 is

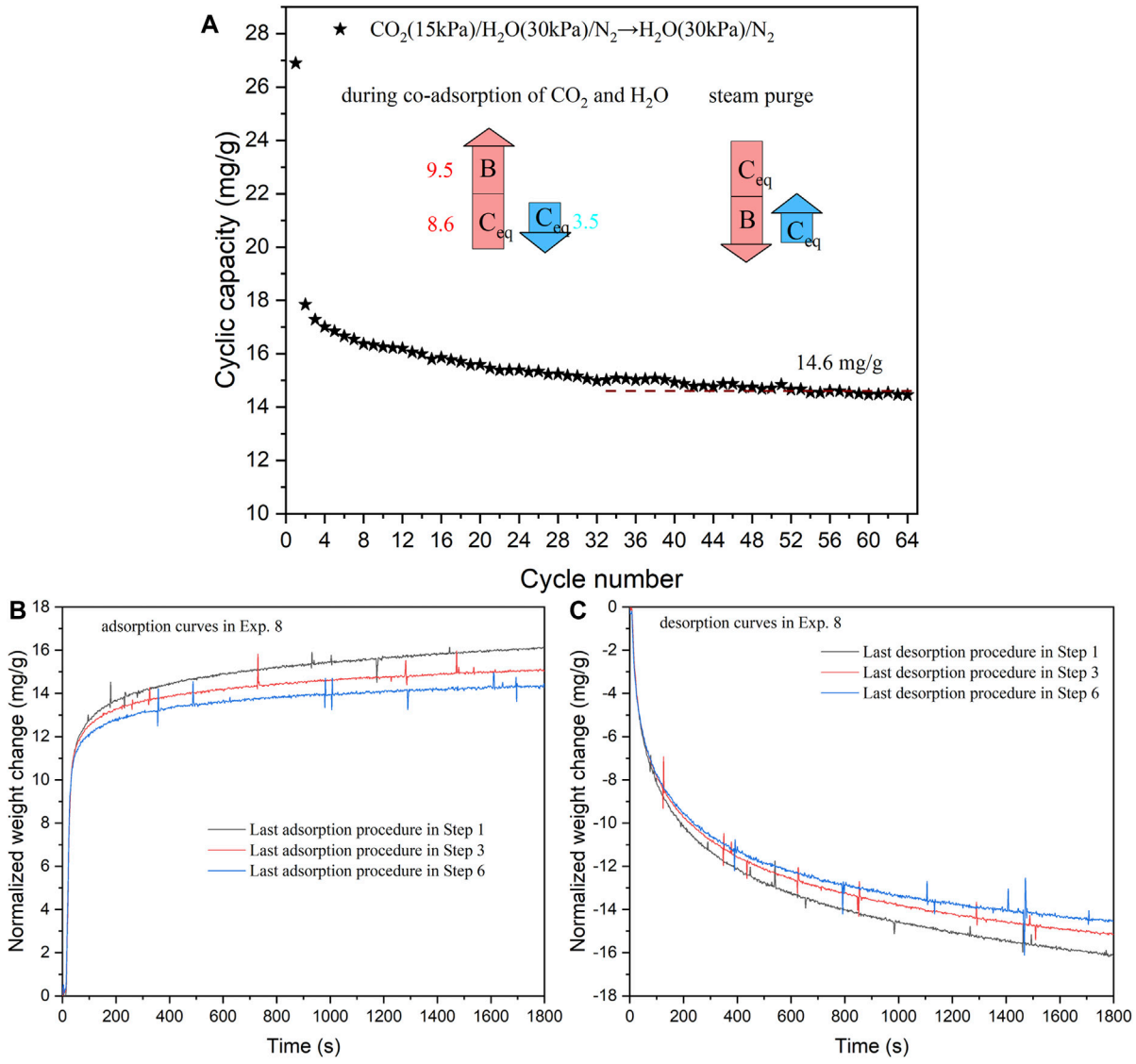

FIGURE 9
(A) Cyclic capacities of all the cycles in Exp. 8 (co-adsorption of CO_2 and H_2O/steam purge on KMG30 at 400 °C). **(B)** Adsorption kinetics of the last procedures in Steps 1, 3 and 6 (Exp. 8). **(C)** Desorption kinetics of the last procedures in Steps 1, 3 and 6 (Exp. 8).

utilized. However, under cycles of CO_2 adsorption/steam purge, both Sites B and C are involved (as shown in Figure 5). The same explanation applies to the cycles of CO_2 and H_2O co-adsorption/steam purge, where both Sites B and C contribute to the process (as seen in Figure 9A). In the cycles of CO_2 and H_2O co-adsorption/N_2 flushing, it is hypothesized that during N_2 flushing, the steam desorbed from Site A may assist in removing CO_2 from Site C through Eq. (3). However, this hypothesis requires further validation through breakthrough experiments.

3.6 Performance of MG30, K_2CO_3 and KSORB under adsorption/desorption cycles

Experiment of $[CO_2 \rightarrow N_2 \rightarrow H_2O \rightarrow N_2] \times 6 \Rightarrow [CO_2 \rightarrow H_2O] \times 40 \Rightarrow [CO_2 \rightarrow N_2] \times 50$ was conducted using MG30, KSORB and K_2CO_3. For K_2CO_3, negligible weight changes were observed throughout the long test due to its very low surface area. In the cycles of $[CO_2 \rightarrow N_2 \rightarrow H_2O \rightarrow N_2]$, as shown in Supplementary Figure S6A, B, Sites A, B, and C were applicable to KSORB but not to MG30. MG30, on the other hand, exhibited behavior more consistent with being a sorbent for H_2O adsorption rather than CO_2 adsorption, as evidenced by the cycles of $[CO_2 \rightarrow H_2O]$ (see Supplementary Figure S6C). Further breakthrough experiments are necessary to elucidate and quantify the behavior of MG30 during the cycles of $[CO_2 \rightarrow N_2 \rightarrow H_2O \rightarrow N_2]$.

During the cycles of $[CO_2 \rightarrow N_2]$, KSORB exhibited higher cyclic capacities than MG30, but lower than KMG30 (see Figure 2A). This can be attributed to the ability of K_2CO_3 to create basic sites for CO_2 adsorption through its interaction with MgO and Al_2O_3 on potassium-promoted layered double oxides (Veselovskaya et al., 2013; Zhu et al., 2019). Similar to KMG30, the CO_2 capacities (in Site B) rapidly decreased for KSORB during the first 20 cycles of $[CO_2 \rightarrow N_2]$. Weight loss was less pronounced for MG30. Thus, the

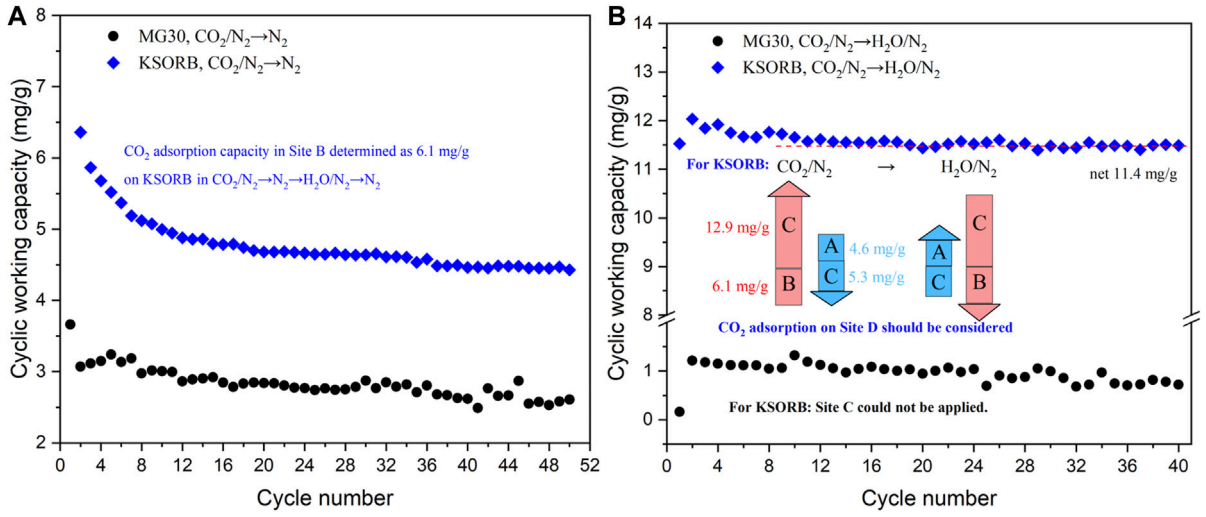

FIGURE 10
Cyclic capacities on MG30 and KSORB for 50 cycles of [$CO_2 \rightarrow N_2$] (subfigure **(A)**) and for 40 cycles of [$CO_2 \rightarrow H_2O$] (subfigure **(B)**).

sites created by K_2CO_3 could be a contributing factor to the capacity loss. Within the cycles of [$CO_2 \rightarrow H_2O$], stable cyclic capacities were observed for both MG30 and KSORB (see Figure 10).

4 Characterizations of hydrotalcite after different adsorption/desorption cycles

The aim is to understand how many repeated adsorption and desorption processes impact the morphology of KMG30. In Section 4.1, the effects of H_2O adsorption/N_2 flushing on the structural changes of KMG30 and whether the KMG30 is capable of reconstruction are presented. In Section 4.2, structural changes and changes in surface areas and pore size distributions of KMG30 under various adsorption/desorption cycles are examined.

4.1 Effects of H_2O adsorption/N_2 flushing cycles on morphological changes of KMG30

To investigate the effects and changes in the morphology of KMG30, various characterization techniques were employed, where one should keep in mind that restructuring of the sorbent can take place during cooling down at the end of the experiment. Initially, SEM images were taken to examine the morphological changes of KMG30 after exposure to cycles of [$H_2O \rightarrow N_2$] and cycles of [$CO_2/H_2O \rightarrow N_2$]. However, as shown in Supplementary Figure S7, there were minimal differences observed in the SEM images. However, this may also indicate that SEM may not be suitable for accurately assessing the morphological changes in KMG30. Based on our assumption, the sites created by K_2CO_3 could be the reason for the capacity loss in Section 3.2.

EDX and ICP-MS analyses were conducted to further understand the distribution of K_2CO_3 on the surface of KMG30. The results obtained from the EDX and ICP-MS analyses were found to be consistent. EDX analysis (details see Supplementary Table S3) is used to investigate the elemental composition of solid surfaces and ICP-MS technique is used to analyze the overall concentration of a sample. The results, with no significant difference between the surface (EDX) and bulk (ICP-MS) concentrations of K, Al, and Mg, suggest that K_2CO_3 is distributed throughout the entire sorbent, including both the pores and surfaces of KMG30.

Notably, EDX point analysis was performed on 10 selected points on the surface of KMG30. The mean composition of these points was summarized in Supplementary Table S4. It was observed that the standard deviations, represented by the signs (±), became larger when KMG30 was exposed to cycles of [$H_2O \rightarrow N_2$]. This suggests that the treatment with cycles of [$H_2O \rightarrow N_2$] led to more heterogeneous distribution of K_2CO_3 and Al_2O_3 on the surface of KMG30. However, it is important to note that KMG30 was found to be a heterogeneous sorbent, as evident from the varying color depths observed in the EDX analysis (Supplementary Figure S7D). Therefore, drawing conclusive interpretations solely based on the analytical results obtained by EDX may not be convincing. The XRD technique was employed to determine any alterations in the crystal structure of KMG30 and provide valuable insights into the structural changes in KMG30 following different treatment cycles.

4.1.1 The aggregation of K_2CO_3 from KMG30 under cycles of H_2O adsorption/N_2 flushing

The XRD patterns of fresh KMG30 before calcination are shown in Supplementary Figure S8A, where several peaks are identified as K-dawsonite (ICDD No. 21-0979). The fresh KMG30, which was kept in a container exposed to air for over 4 years, naturally contains K-dawsonite due to its formation on a sorbent composed of K_2CO_3 and Al_2O_3 at room temperature in air (Lee et al., 2006; Veselovskaya et al., 2013). However, it can be fully regenerated at 673.15 K (Lee et al., 2006). The characteristic peaks of K-dawsonite are not observed in Supplementary Figure S8B, indicating successful calcination of KMG30, as confirmed by comparing its XRD patterns with those reported in literature (Maroño et al., 2013). The XRD patterns for MG30 can be found in Supplementary Figure S8C.

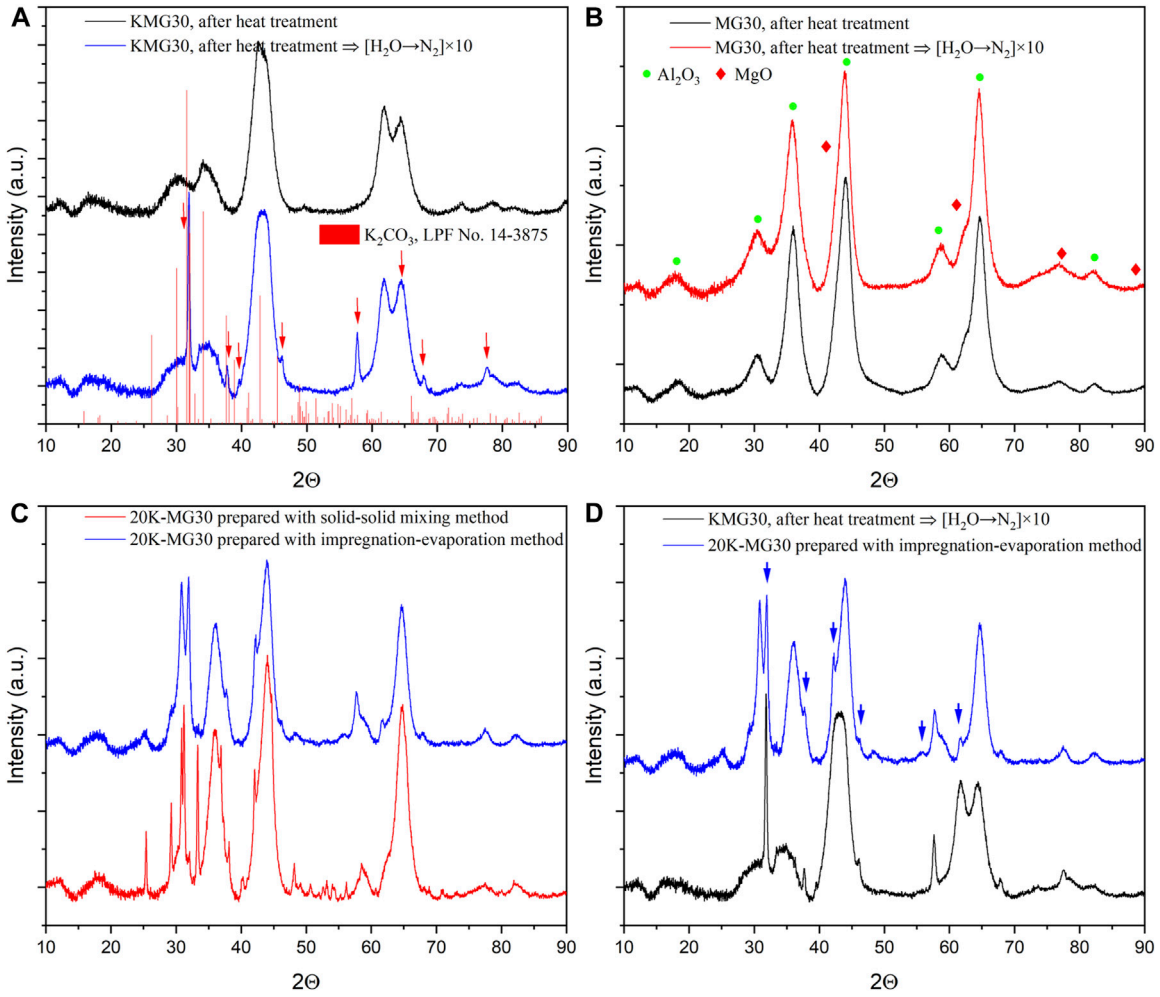

FIGURE 11
(A) Comparison of XRD patterns for heat-treated KMG30 before and after 10 cycles of H_2O adsorption/N_2 flushing. **(B)** Comparison of XRD patterns for heat-treated MG30 before and after 10 cycles of H_2O adsorption/N_2 flushing. **(C)** Comparison of XRD patterns for the 20K-MG30 prepared with solid-solid mixing and impregnation-evaporation methods. **(D)** XRD patterns for the 20K-MG30 prepared with impregnation-evaporation method in comparison with the ones for the treated KMG30 (after 10 cycles of H_2O adsorption/N_2 flushing).

Interesting findings have been made regarding the XRD patterns of KMG30 after treatment with 10 cycles of H_2O adsorption/N_2 flushing. In Figure 11A, new peaks, indicated by red arrows, have been observed and identified as K_2CO_3. A comparison is presented in Supplementary Figure S10C, between the XRD patterns of anhydrous K_2CO_3 and the new peaks observed on KMG30. To further investigate these peaks, a comparison was made with XRD patterns of other potential candidates, including brucite, Al_2O_3, MgO, spinel ($MgAl_2O_4$) and hydrotalcite, as shown in Supplementary Figures S9A–D. Brucite and spinel were excluded based on their thermal stabilities, considering that brucite mostly decomposes in N_2 at 673.15 K (Liu et al., 2018), and spinel is rarely formed below 973.15 K (Hibino and Tsunashima, 1997).

The aggregation of K_2CO_3 from KMG30 was confirmed through experiments with MG30. In Figure 11B, the XRD pattern of MG30 shows no changes in characteristic peaks when exposed to 10 cycles of steam adsorption/N_2 flushing. The appearance of new peaks in the XRD pattern of KMG30 after steam adsorption/N_2 flushing cycles (Supplementary Figure S9A) may be attributed to the altered dispersion of K_2CO_3 on MG30. Two methods, solid-solid mixing and impregnation-evaporation, were employed to prepare MG30 with 20 wt % K_2CO_3 loading (Section 2.1). The XRD patterns of the resulting materials, as shown in Figure 11C, demonstrate that the number of peaks is significantly lower in the 20K-MG30 prepared with the latter method. The peaks labeled with blue arrows in Figure 11D correspond to the same 2θ values as the new peaks observed for KMG30 after H_2O adsorption/N_2 flushing cycles. Furthermore, for the 20K-MG30, the new peaks become less pronounced after 20 cycles of CO_2 and H_2O co-adsorption/N_2 flushing (Supplementary Figure S10B). These findings suggest that the emergence of the new peaks is due to a less even distribution of K_2CO_3 on MG30 after H_2O adsorption/N_2 flushing cycles, and this distribution can be altered by subjecting the potassium-promoted hydrotalcite to specific adsorption/desorption cycles.

4.1.2 The reversibility of the K_2CO_3 aggregation on KMG30

The investigation focused on whether the aggregated K_2CO_3 from KMG30 could be re-dispersed. After subjecting

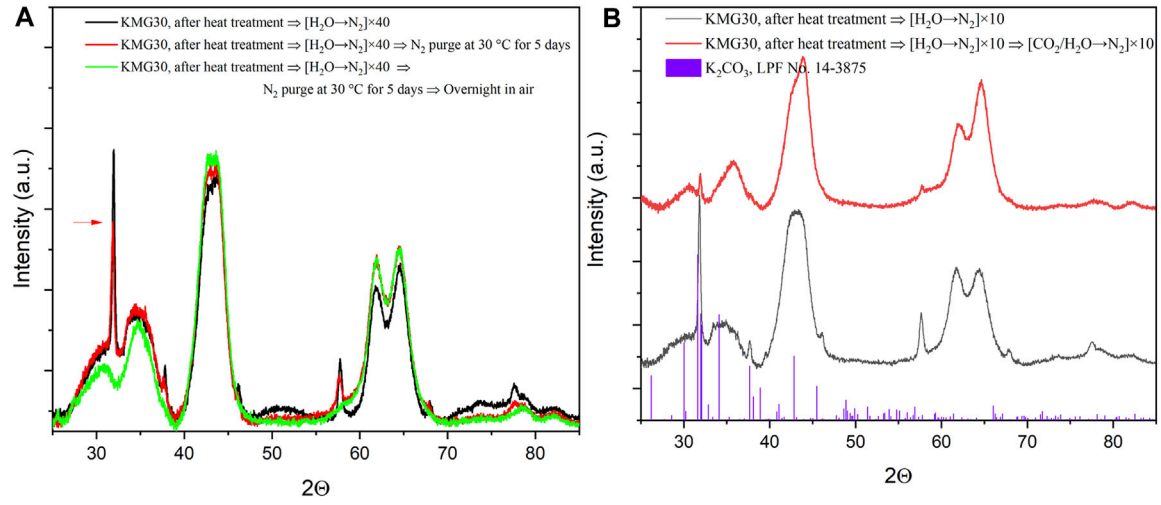

FIGURE 12
Comparisons of XRD patterns for the treated samples of KMG30, including samples of **(A)** aggregated KMG30 before and after N_2 flushing as well after being placed in air, **(B)** aggregated KMG30 before and after treated with cycles of [CO_2/H_2O→N_2].

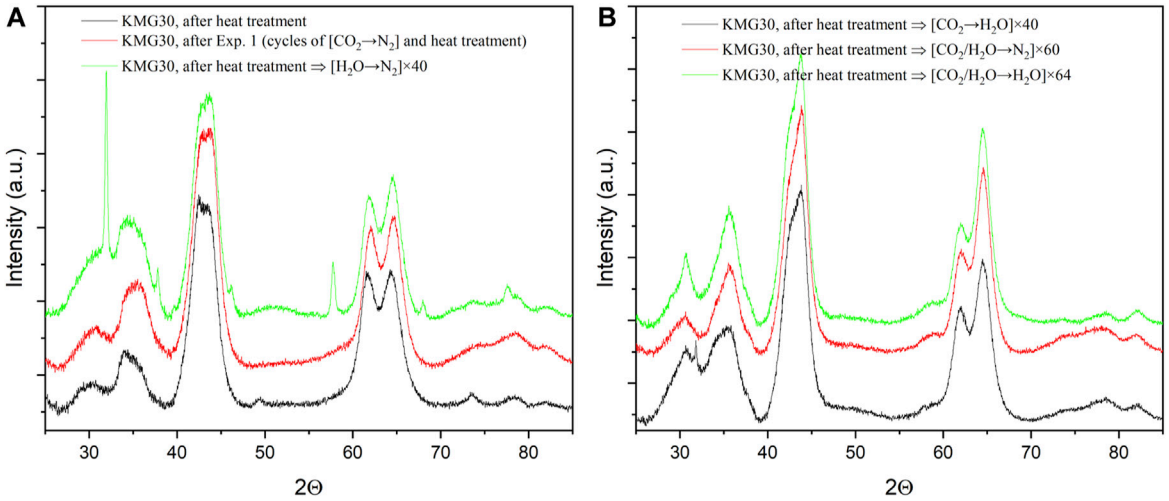

FIGURE 13
Comparisons of XRD patterns for the treated samples of KMG30, including **(A)** samples of heat-treated KMG30, heat-treated KMG30 after multi-cycles of [CO_2→N_2] and heat-treated KMG30 after 40 cycles of [H_2O→N_2], **(B)** samples of heat-treated KMG30 after 40 cycles of [CO_2→H_2O], heat-treated KMG30 after 60 cycles of [CO_2/H_2O→N_2] and heat-treated KMG30 after 64 cycles of [CO_2/H_2O→H_2O].

KMG30 samples to heat treatment and cycles of [H_2O→N_2] within the TGA setup, the resulting samples, referred to as aggregated KMG30, were further treated using different procedures. The gas species in the adsorption and desorption cycles matter much more than their partial pressures according to our proved adsorption mechanism. XRD analysis showed no changes in the XRD patterns when the aggregated KMG30 was subjected to additional heat treatment or cycles of [CO_2→N_2], as depicted in Supplementary Figure S11A, B. The reconstruction behavior of Mg-Al hydrotalcites upon contact with water vapor in N_2 was extensively studied (Pérez-Ramírez et al., 2007). This was also confirmed by the green curves in Figure 12A, where the narrow and sharp peaks disappeared when the aggregated KMG30 was exposed to air overnight. However, the sharp peaks showed slight changes with continuous N_2 purging for 5 days. In the case of KMG30, after cycles of [H_2O→N_2], H_2O was chemisorbed in Site C, which aided in partial reconstruction of the hydrotalcite structure. The slow reconstruction rate could be attributed to insufficient steam or CO_2 amounts in the gas phase. Marta et al. reported that the presence of CO_2 defects in the reaction media could limit the reconstruction of K-doped hydrotalcite-based sorbents, and an optimum ratio of PCO_2/PH_2O is necessary for complete reconstruction (Maroño et al., 2013). After cycles of [CO_2/H_2O→N_2], both CO_2 and H_2O were chemisorbed in Site C. The red curves in Figure 12B show that the sharp peaks were significantly weakened, indicating that CO_2 also plays an important role in the reconstruction of the sorbent.

4.2 Effect of other working cycles on the morphological change of KMG30

The effects of other working cycles including [CO_2→N_2], [CO_2→H_2O], [CO_2/H_2O→N_2] and [CO_2/H_2O→H_2O] on the morphological changes of KMG30 were investigated using XRD. The results, as depicted in Figure 13, show no significant changes in the XRD patterns when the heat-treated KMG30 is subjected to cycles of [CO_2→N_2], heat treatment, cycles of [CO_2/H_2O→N_2], and cycles of [CO_2/H_2O→H_2O]. The effects of cycles of [H_2O→N_2] have already been discussed in Section 4.1, as represented by the green curves in Figure 13A. However, when the heat-treated KMG30 is processed with cycles of [CO_2→H_2O], a small peak is observed at a 2-theta value around 32°, indicating some minor structural changes that warrant further investigation.

The morphological changes of KMG30 were also analyzed using BET surface area analysis. The results, presented in Supplementary Table S5, show that the surface areas of KMG30 exhibit only slight changes when subjected to different working cycles. While surface area is an important property for an adsorbent, these slight changes do not fully explain the observed capacity loss when KMG30 is exposed to cycles of [H_2O→N_2]. To further investigate the pore size distributions, the BJH method was employed, and the results are displayed in Supplementary Figure S12. Overall, it can be observed that the pore sizes tend to increase after different treatments. Specifically, the pore volumes decrease for pores with sizes smaller than 4 nm, while the pore volumes increase for pores with sizes larger than 8 nm. However, when the heat-treated KMG30 is treated with cycles of [H_2O→N_2], as shown in Figure 11A, it is unlikely that the closure of nanopores with sizes less than 4 nm is responsible for the aggregation of K_2CO_3, considering the small pore volumes of these nanopores (<0.008 cm^3/g). It should be noted that it is challenging to speculate on the morphological changes of the sorbent under working cycles (at 400 °C) using *ex-situ* analyses alone. Therefore, it is recommended to use *in-situ* TEM (transmission electron microscopy) for future studies to gain more insight into the morphological changes of KMG30.

5 Conclusion

KMG30 demonstrates stability in both structure and sorption capacity when subjected to cycles of [CO_2→H_2O], cycles of [CO_2/H_2O→N_2] and cycles of [CO_2/H_2O→H_2O]. Although slight differences in XRD patterns can be observed for KMG30 processed with these procedures, the sorption capacities remain stable over many repeated cycles of adsorption and desorption due to the relatively fast desorption kinetics. However, when KMG30 is exposed to cycles of [H_2O→N_2], a loss in capacity for CO_2 adsorption occurs due to the aggregation of K_2CO_3 on the sorbent. This aggregation can be reversed by re-dispersing the K_2CO_3 either by exposure to air or by processing the sorbent with cycles of [CO_2/H_2O→N_2]. In the case of the most used cycles of [CO_2→N_2] in literature study, there also a continuous decline in the cyclic capacity for CO_2 over time is observed, even with intermittent heat treatment. This capacity loss can be attributed to the partial regeneration of Site C, which is likely associated with K_2CO_3 modification on MG30. To investigate the morphological changes of KMG30 under different working cycles, BET and SEM-EDX analyses were performed. However, these *ex-situ* techniques did not reveal any significant differences. Nevertheless, these results contribute to a better understanding of the stability of KMG30 and can inform the design of sorption processes for maximal stable cyclic working capacity of CO_2 on potassium-promoted hydrotalcites.

Data availability statement

The original contributions presented in the study are included in the article/Supplementary Material, further inquiries can be directed to the corresponding author.

Author contributions

KX: Conceptualization, Data curation, Formal Analysis, Investigation, Methodology, Software, Validation, Visualization, Writing–original draft. JB: Conceptualization, Funding acquisition, Methodology, Project administration, Supervision, Writing–review and editing. HD: Conceptualization, Methodology, Supervision, Writing–review and editing. MA: Conceptualization, Funding acquisition, Methodology, Project administration, Resources, Supervision, Writing–review and editing.

Funding

The author(s) declare financial support was received for the research, authorship, and/or publication of this article. This project has received funding from the Dutch Ministry for Economic Affairs and Climate Policy through TNO.

Conflict of interest

The authors declare that the research was conducted in the absence of any commercial or financial relationships that could be construed as a potential conflict of interest.

The author(s) declared that they were an editorial board member of Frontiers, at the time of submission. This had no impact on the peer review process and the final decision.

Publisher's note

Supplementary material

The Supplementary Material for this article can be found online at: https://www.frontiersin.org/articles/10.3389/fceng.2024.1272152/full#supplementary-material

References

Boon, J., Cobden, P. D., van Dijk, H. A. J., and van Sint Annaland, M. (2015). High-temperature pressure swing adsorption cycle design for sorption-enhanced water–gas shift. *Chem. Eng. Sci.* 122, 219–231. doi:10.1016/J.CES.2014.09.034

Boon, J., Spallina, V., van Delft, Y., and van Sint Annaland, M. (2016). Comparison of the efficiency of carbon dioxide capture by sorption-enhanced water–gas shift and palladium-based membranes for power and hydrogen production. *Int. J. Greenh. Gas. Control* 50, 121–134. doi:10.1016/J.IJGGC.2016.04.033

Cobden, P. D., van Beurden, P., Reijers, H. T. J., Elzinga, G. D., Kluiters, S. C. A., Dijkstra, J. W., et al. (2007). Sorption-enhanced hydrogen production for pre-combustion CO2 capture: thermodynamic analysis and experimental results. *Int. J. Greenh. Gas. Control* 1, 170–179. doi:10.1016/S1750-5836(07)00021-7

Coenen, K., Gallucci, F., Cobden, P., van Dijk, E., Hensen, E., and van Sint Annaland, M. (2016). Chemisorption working capacity and kinetics of CO2 and H2O of hydrotalcite-based adsorbents for sorption-enhanced water-gas-shift applications. *Chem. Eng. J.* 293, 9–23. doi:10.1016/J.CEJ.2016.02.050

Coenen, K., Gallucci, F., Cobden, P., van Dijk, E., Hensen, E., and van Sint Annaland, M. (2018). Influence of material composition on the CO2 and H2O adsorption capacities and kinetics of potassium-promoted sorbents. *Chem. Eng. J.* 334, 2115–2123. doi:10.1016/J.CEJ.2017.11.161

Coenen, K., Gallucci, F., Pio, G., Cobden, P., van Dijk, E., Hensen, E., et al. (2017). On the influence of steam on the CO2 chemisorption capacity of a hydrotalcite-based adsorbent for SEWGS applications. *Chem. Eng. J.* 314, 554–569. doi:10.1016/J.CEJ.2016.12.013

Ebrahimi, P., Kumar, A., and Khraisheh, M. (2020). A review of recent advances in water-gas shift catalysis for hydrogen production. *Emergent Mater* 3, 881–917. doi:10.1007/s42247-020-00116-y

Hibino, T., and Tsunashima, A. (1997). Formation of spinel from a hydrotalcite-like compound at low temperature: reaction between edges of crystallites. *Clays Clay Min.* 45, 842–853. doi:10.1346/CCMN.1997.0450608

Hu, X., Liu, L., Luo, X., Xiao, G., Shiko, E., Zhang, R., et al. (2020a). A review of N-functionalized solid adsorbents for post-combustion CO2 capture. *Appl. Energy* 260, 114244. doi:10.1016/J.APENERGY.2019.114244

Hu, X., Luo, X., Xiao, G., Yu, Q., Cui, Y., Zhang, G., et al. (2020b). Low-cost novel silica@polyacrylamide composites: fabrication, characterization, and adsorption behavior for cadmium ion in aqueous solution. *Adsorption* 26, 1051–1062. doi:10.1007/s10450-020-00225-4

Hufton, J. R., Mayorga, S., and Sircar, S. (1999). Sorption-enhanced reaction process for hydrogen production. *AIChE J.* 45, 248–256. doi:10.1002/AIC.690450205

Jansen, D., Van Selow, E., Cobden, P., Manzolini, G., Macchi, E., Gazzani, M., et al. (2013). SEWGS technology is now ready for scale-up. *Energy Procedia* 37, 2265–2273. doi:10.1016/J.EGYPRO.2013.06.107

Lee, S. C., Choi, B. Y., Lee, T. J., Ryu, C. K., Ahn, Y. S., and Kim, J. C. (2006). CO2 absorption and regeneration of alkali metal-based solid sorbents. *Catal. Today* 111, 385–390. doi:10.1016/J.CATTOD.2005.10.051

Liu, C., Liu, T., and Wang, D. (2018a). Non-isothermal kinetics study on the thermal decomposition of brucite by thermogravimetry. *J. Therm. Anal. Calorim.* 134, 2339–2347. doi:10.1007/s10973-018-7654-4

Liu, L., Chen, H., Shiko, E., Fan, X., Zhou, Y., Zhang, G., et al. (2018b). Low-cost DETA impregnation of acid-activated sepiolite for CO2 capture. *Chem. Eng. J.* 353, 940–948. doi:10.1016/J.CEJ.2018.07.086

Manzolini, G., MacChi, E., and Gazzani, M. (2013). CO2 capture in integrated gasification combined cycle with SEWGS – Part B: economic assessment. *Fuel* 105, 220–227. doi:10.1016/J.FUEL.2012.07.043

Maroño, M., Torreiro, Y., and Gutierrez, L. (2013). Influence of steam partial pressures in the CO2 capture capacity of K-doped hydrotalcite-based sorbents for their application to SEWGS processes. *Int. J. Greenh. Gas. Control* 14, 183–192. doi:10.1016/J.IJGGC.2013.01.024

Maroño, M., Torreiro, Y., Montenegro, L., and Sánchez, J. (2014). Lab-scale tests of different materials for the selection of suitable sorbents for CO2 capture with H2 production in IGCC processes. *Fuel* 116, 861–870. doi:10.1016/J.FUEL.2013.03.067

Martunus, S., Helwani, Z., Wiheeb, A. D., Kim, J., and Othman, M. R. (2012). Improved carbon dioxide capture using metal reinforced hydrotalcite under wet conditions. *Int. J. Greenh. Gas. Control* 7, 127–136. doi:10.1016/J.IJGGC.2012.01.007

Miguel, C. V., Trujillano, R., Rives, V., Vicente, M. A., Ferreira, A. F. P., Rodrigues, A. E., et al. (2014). High temperature CO2 sorption with gallium-substituted and promoted hydrotalcites. *Sep. Purif. Technol.* 127, 202–211. doi:10.1016/J.SEPPUR.2014.03.007

Nuttall, W. J., and Bakenne, A. T. (2020). Introduction—the hydrogen economy today. *Foss. Fuel Hydrog.* 2020, 1–14. doi:10.1007/978-3-030-30908-4_1

Pérez-Ramírez, J., Abelló, S., and Van Der Pers, N. M. (2007). Memory effect of activated Mg–Al hydrotalcite: *in situ* XRD studies during decomposition and gas-phase reconstruction. *Chem. – A Eur. J.* 13, 870–878. doi:10.1002/CHEM.200600767

Rocha, C., Soria, M. A., and Madeira, L. M. (2019). Effect of interlayer anion on the CO2 capture capacity of hydrotalcite-based sorbents. *Sep. Purif. Technol.* 219, 290–302. doi:10.1016/J.SEPPUR.2019.03.026

Rossi, T. M., Campos, J. C., and Souza, M. M. V. M. (2016). CO2 capture by Mg–Al and Zn–Al hydrotalcite-like compounds. *Adsorption* 22, 151–158. doi:10.1007/s10450-015-9732-2

Silva, J. M., Trujillano, R., Rives, V., Soria, M. A., and Madeira, L. M. (2017). High temperature CO2 sorption over modified hydrotalcites. *Chem. Eng. J.* 325, 25–34. doi:10.1016/J.CEJ.2017.05.032

Song, H., Liu, Y., Bian, H., Shen, M., and Lin, X. (2022). Energy, environment, and economic analyses on a novel hydrogen production method by electrified steam methane reforming with renewable energy accommodation. *Energy Convers. Manag.* 258, 115513. doi:10.1016/J.ENCONMAN.2022.115513

Sun, L., Yang, Y., Ni, H., Liu, D., Sun, Z., Li, P., et al. (2020). Enhancement of CO2 adsorption performance on hydrotalcites impregnated with alkali metal nitrate salts and carbonate salts. *Ind. Eng. Chem. Res.* 59, 6043–6052. doi:10.1021/acs.iecr.9b05700

van Selow, E. R., Cobden, P. D., van den Brink, R. W., Hufton, J. R., and Wright, A. (2009a). Performance of sorption-enhanced water-gas shift as a pre-combustion CO2 capture technology. *Energy Procedia* 1, 689–696. doi:10.1016/J.EGYPRO.2009.01.091

Van Selow, E. R., Cobden, P. D., Verbraeken, P. A., Hufton, J. R., and Van Den Brink, R. W. (2009b). Carbon capture by sorption-enhanced water-gas shift reaction process using hydrotalcite-based material. *Ind. Eng. Chem. Res.* 48, 4184–4193. doi:10.1021/ie801713a

Veselovskaya, J. V., Derevschikov, V. S., Kardash, T. Y., Stonkus, O. A., Trubitsina, T. A., and Okunev, A. G. (2013). Direct CO2 capture from ambient air using K2CO3/Al2O3 composite sorbent. *Int. J. Greenh. Gas. Control* 17, 332–340. doi:10.1016/J.IJGGC.2013.05.006

Walspurger, S., Boels, L., Cobden, P. D., Elzinga, G. D., Haije, W. G., and Van Den Brink, R. W. (2008). The crucial role of the K+–Aluminium oxide interaction in K+-Promoted alumina- and hydrotalcite-based materials for CO2 sorption at high temperatures. *ChemSusChem* 1, 643–650. doi:10.1002/CSSC.200800085

Wang, J., Huang, L., Yang, R., Zhang, Z., Wu, J., Gao, Y., et al. (2014). Recent advances in solid sorbents for CO 2 capture and new development trends. *Energy Environ. Sci.* 7, 3478–3518. doi:10.1039/C4EE01647E

Wu, Y. J., Li, P., Yu, J. G., Cunha, A. F., and Rodrigues, A. E. (2013). K-promoted hydrotalcites for CO2 capture in sorption enhanced reactions. *Chem. Eng. Technol.* 36, 567–574. doi:10.1002/CEAT.201200694

Xiao, P. W., Jun, J. Y., Cheng, J., Zheng, P. H., and Zhi, P. X. (2008). High-temperature adsorption of carbon dioxide on mixed oxides derived from hydrotalcite-like compounds. *Environ. Sci. Technol.* 42, 614–618. doi:10.1021/es072085a

Zhu, X., Chen, C., Wang, Q., Shi, Y., O'Hare, D., and Cai, N. (2019). Roles for K2CO3 doping on elevated temperature CO2 adsorption of potassium promoted layered double oxides. *Chem. Eng. J.* 366, 181–191. doi:10.1016/J.CEJ.2019.01.192